Application of FUN3D and CFL3D to the Third Workshop on CFD Uncertainty Analysis

Christopher L. Rumsey and James L. Thomas

NASA Langley Research Center, Hampton, VA 23681-2199, USA

Two Reynolds-averaged Navier-Stokes computer codes – one unstructured and one structured – are applied to two workshop cases for the purpose of uncertainty analysis. The Spalart-Allmaras turbulence model is employed. The first case uses the method of manufactured solution and is intended as a verification case. In other words, the CFD solution is expected to approach the exact solution as the grid is refined. The second case is a validation case (comparison against experiment), for which modeling errors inherent in the turbulence model and errors/uncertainty in the experiment may prevent close agreement. The results from the two computer codes are also compared. This exercise verifies that the codes are consistent both with the exact manufactured solution and with each other. In terms of order property, both codes behave as expected for the manufactured solution. For the backward facing step, CFD uncertainty on the finest grid is computed and is generally very low for both codes (whose results are nearly identical). Agreement with experiment is good at some locations for particular variables, but there are also many areas where the CFD and experimental uncertainties do not overlap.

I. Description of the Computer Codes

FUN3D[1–3] is a finite-volume RANS solver (either compressible or incompressible equations can be solved) in which the flow variables are generally stored at the vertices of the mesh. FUN3D solves the equations on mixed element grids, including tetrahedra, pyramids, prisms, and hexahedra and also has a two-dimensional path. It employs an implicit upwind algorithm in which the inviscid fluxes are obtained with a flux-splitting scheme. At interfaces delimiting neighboring control volumes, the inviscid fluxes are computed using an approximate Riemann solver based on the values on either side of the interface. For second-order accuracy, interface values are obtained by extrapolation using gradients computed at the mesh vertices using an unweighted least-squares technique. Limiting of the reconstructed values may be employed for flows with strong shocks. For all results presented in this paper, the convective flux scheme used is Roe's flux difference splitting.[4] For tetrahedral meshes, the full viscous fluxes are discretized using a finite-volume formulation in which the required velocity gradients on the dual faces are computed using the Green-Gauss theorem. On tetrahedral meshes this is equivalent to a Galerkin type approximation. For non-tetrahedral meshes, edge-based gradients are combined with Green-Gauss gradients, which improves the h-ellipticity of the operator, and the complete viscous stresses are evaluated. The solution at each time-step is updated with a backward Euler time-differencing scheme. At each time step, the linear system of equations is approximately solved with either a multi-color point-implicit procedure or an implicit-line relaxation scheme.[5] Local time-step scaling is employed to accelerate convergence to steady-state. FUN3D is able to solve the RANS flow equations, either coupled or uncoupled with the Spalart-Allmaras[6] (SA) one-equation turbulence model. The Menter SST Model[7] is also available for uncoupled solutions. In this paper all computations are uncoupled and use the SA model. By default, the turbulence advection terms are discretized using first-order upwinding.

An emerging capability in FUN3D is the ability to solve with a cell-centered discretization instead of node-centered. Although this capability is not fully production-ready at this time, some preliminary results will be shown for the manufactured solution. Also, in these cell-centered solutions, the turbulence advection terms are discretized with a conservative second-order accurate scheme.

CFL3D is a structured-grid upwind multi-zone CFD code that solves the generalized thin-layer or full Navier-Stokes equations.[8] For all results in this paper, the full Navier-Stokes equations have been employed. The code can use point-matched, patched, or overset grids and employs local time-step scaling, grid sequencing and multigrid to accelerate convergence to steady stage. A time-accurate mode is available, and the code can employ low-Mach number preconditioning for accuracy in computing low-speed steady-state flows. CFL3D is a cell-centered finite-volume method. It uses third-order upwind-biased spatial differencing on the convective and pressure terms, and

second-order differencing on the viscous terms. Roe's flux difference-splitting (FDS) method[4] is used to obtain fluxes at the cell faces. The solution is advanced in time with an implicit approximate factorization method. A wide variety of eddy-viscosity turbulence models are available in the code, including nonlinear models. Only SA has been used in this study. Cross-derivative terms are ignored in the turbulence model. The turbulence models are solved uncoupled from the mean flow equations, and, unless otherwise specified by the user, are solved with first-order upwind turbulence advection terms.

II. Discretization Uncertainty Estimation

The current procedure for the estimation of discretization uncertainty is based on the grid convergence index (GCI) from Celik et al.[9] The GCI on the fine grid is given by:

$$GCI^{21} = \frac{1.25 e_a^{21}}{(r_{21})^p - 1} \tag{1}$$

where

$$e_a^{21} = \left| \frac{\phi_1 - \phi_2}{\phi_1} \right| \tag{2}$$

and ϕ_1 is the quantity of interest on the finest grid, ϕ_2 is the quantity of interest on the next-finest grid, r_{21} is the ratio of cell spacing from one grid to the next, and p is the order of accuracy of the method.

In the current paper, the grids are all structured (solved as mixed-element type hexahedra in the unstructured code), and successively coarser levels are constructed by removing every other grid point in each coordinate direction. Thus, $r_{21} = 2$ for all results herein. When three grid levels are available and $r_{21} = r_{32} = 2$, the order p is computed from:

$$p = \frac{1}{ln(2)} \left(ln(\varepsilon_{32}/\varepsilon_{21}) \right) \tag{3}$$

where $\varepsilon_{32} = \phi_3 - \phi_2$ and $\varepsilon_{21} = \phi_2 - \phi_1$. When the quantity $\varepsilon_{32}/\varepsilon_{21} < 0$, the convergence is said to be "oscillatory," and when $|\varepsilon_{32}| < |\varepsilon_{21}|$ the sequence is "divergent." In either case, eq. (3) no longer applies.

The discretization uncertainty, U, of the solution on the fine grid is defined by:

$$U = GCI^{21} |\phi_1| \tag{4}$$

However, as Eca and Hoekstra[10] point out, if $p < 1$, uncertainty estimates tend to be over-conservative, and, for p much higher than the theoretical order of the method, the uncertainty estimates can be unreliable. Therefore, we adopt the following methodology for estimating the uncertainty (some of these ideas are from Eca and Hoekstra):

- For $0.95 \leq p < 3.05$, $U = GCI^{21} |\phi_1|$
- For $0 < p < 0.95$: $U = min(GCI^{21} |\phi_1| \, , 1.25 \Delta_M)$
- For $p \geq 3.05$: $U = max(GCI^{*21} |\phi_1| \, , 1.25 \Delta_M)$

where Δ_M is the maximum difference in absolute value between the ϕ_i on any of the three grid levels used to determine p, and GCI^{*21} is the same as eq. (1) except that p is taken to be 3:

$$GCI^{*21} = \frac{1.25 e_a^{21}}{(r_{21})^3 - 1} \tag{5}$$

For oscillatory convergence, the uncertainty is taken as: $U = GCI^{**21} |\phi_1|$, where a presumed order of convergence $p = 2$ is assumed, and a higher factor of safety is employed (2.5 as opposed to 1.25):

$$GCI^{**21} = \frac{2.5 e_a^{21}}{(r_{21})^2 - 1} \tag{6}$$

For divergence ($|\varepsilon_{32}| < |\varepsilon_{21}|$), the uncertainty is taken as $U = 3 \Delta_M$.

III. Manufactured Solution

The manufactured solution used is the same as that described as MS1 in Eca et al.[11] for flow on a square domain $0.5L \le x \le L$ and $0 \le y \le 0.5L$, namely:

$$u/u_{ref} = erf(\eta) \tag{7}$$

$$v/u_{ref} = \frac{1}{\sigma\sqrt{\pi}}\left(1 - e^{-\eta^2}\right) \tag{8}$$

$$\frac{p}{\rho u_{ref}^2} = 0.5ln(2x - x^2 + 0.25)ln(4y^3 - 3y^2 + 1.25) \tag{9}$$

$$\tilde{\nu} = \tilde{\nu}_{max}\sqrt{2}\eta_\nu e^{0.5-\eta_\nu^2} \tag{10}$$

where $\eta = \sigma y/x$, $\sigma = 4$, $\eta_\nu = \sigma_\nu y/x$, $\sigma_\nu = 2.5\sigma$, and $\tilde{\nu}_{max} = 10^3\nu$. The Reynolds number $Re = u_{ref}L/\nu = 10^6$. The variable $\tilde{\nu}$ is the turbulence variable from the SA model, which is related to the eddy viscosity ν_t via $\nu_t = \tilde{\nu}f_{v1}$, where $f_{v1} = (\tilde{\nu}/\nu)^3/[(\tilde{\nu}/\nu)^3 + 357.911]$.

Note that FUN3D can be run using incompressible equations, but CFL3D is only a compressible code. When solving the compressible equations, an additional exact solution variable of constant total temperature everywhere in the domain was specified, based on an assumed freestream Mach number of 0.2. Also for the compressible equations it was necessary to scale u, v, and p appropriately.

Although not shown, the codes were also run using the MS2 and MS4 exact solutions, but in these cases the turbulence variable could be driven negative very near the wall over a portion of the domain. This behavior is possibly a result of the fact that these turbulent exact solutions have an asymptotic behavior near the wall that is dramatically different from the generally accepted behavior[12,13] of $\nu_t \propto y^3$. In fact, for MS2: $\nu_t \propto y^8$, and for MS4: $\nu_t \propto y^{16}$. For MS1 the behavior is more reasonable: $\nu_t \propto y^4$. In Eca et al.[11] special handling of the turbulence manufactured source term helped to avoid numerical difficulties; in FUN3D and CFL3D no such special handling was performed.

It should also be pointed out here that the SA model used in FUN3D and CFL3D has minor differences from that employed by Eca et al. In particular, Eca et al. leave out the term f_{t2}, which is a part of the model as specified in Spalart and Allmaras:[6]

$$\frac{\partial\tilde{\nu}}{\partial t} + u_j\frac{\partial\tilde{\nu}}{\partial x_j} = c_{b1}(1 - f_{t2})\hat{S}\tilde{\nu} - \left[c_{w1}f_w - \frac{c_{b1}}{\kappa^2}f_{t2}\right]\left(\frac{\tilde{\nu}}{d}\right)^2 + \frac{1}{\sigma}\left[\frac{\partial}{\partial x_j}\left((\nu + \tilde{\nu})\frac{\partial\tilde{\nu}}{\partial x_j}\right) + c_{b2}\frac{\partial\tilde{\nu}}{\partial x_i}\frac{\partial\tilde{\nu}}{\partial x_i}\right] \tag{11}$$

where

$$f_{t2} = c_{t3}\exp\left(-c_{t4}\chi^2\right) \tag{12}$$

Leaving out the f_{t2} term has a minor influence on the solution behavior. We include the f_{t2} term into our source terms defining the SA exact solution. Also, in FUN3D and CFL3D, an important computational limit is placed on the variable r (which goes into the computation of f_w). The variable r should remain positive to keep the solution well-behaved:

$$r = \frac{\tilde{\nu}}{\hat{S}^*\kappa^2 d^2} \tag{13}$$

where

$$\hat{S}^* = \max\left(\hat{S}, \varepsilon_0\right) \tag{14}$$

$$\hat{S} = \Omega + \frac{\tilde{\nu}}{\kappa^2 d^2}f_{v2} \tag{15}$$

and ε_0 is a very small positive number. It was noticed for MS1 that if $\hat{S}$ is not clipped for eq. (13), the forcing term becomes unbounded at the locations where r passes through zero.

For the manufactured solution, the exact solution was specified along the left, top, and right boundaries for FUN3D (node-centered) and in two rows of ghost-cell centers for CFL3D. For FUN3D (cell-centered), the exact solution and

gradient for the viscous terms were specified along these boundaries. The bottom wall used standard no-slip boundary conditions, with $\partial p/\partial n = 0$ (and, for compressible flow, either $\partial T/\partial n = 0$ in CFL3D or $T =$ constant in FUN3D). The turbulence variable $\tilde{\nu}$ at the wall was set to zero.

Two sets of stretched grids were used. The first set, termed "sg1," had a fine grid size of 577×577. Spacing was uniform in the x-direction ($\Delta x = 0.00086806$), and was stretched in the y-direction. The first grid point off the bottom wall was at $y = 4.3403 \times 10^{-5}$. A total of 5 nested grid levels were employed: 577×577, 289×289, 145×145, 73×73, and 37×37. The second grid set, termed "sg2," had a fine grid size of 289×1153. Spacing was uniform in the x-direction ($\Delta x = 0.00173611$), and was stretched in the y-direction. The first grid point off the bottom wall was at $y = 1 \times 10^{-6}$. A total of 5 nested grid levels were employed: 289×1153, 145×577, 73×289, 37×145, and 19×73.

To determine the discretization error, the exact manufactured source terms were added to the Navier-Stokes equations, and the codes were converged to near machine-zero (10^{-14}) residuals. Various integral and point quantities were compared with the exact solution.

Fig. 1 shows error in drag (from the exact solution $c_d = 16ln(2)\nu/\sqrt{\pi} = 6.25706270620 \times 10^{-6}$) for results on sg1 using the two codes with both first- and second-order turbulence advection terms. The "(cc)" indicates that the cell-centered version of FUN3D was used for one of the runs. In this plot, N represents the total number of degrees of freedom (e.g., number of cell-centers or grid points), so $\sqrt{1/N}$ is a measure of the average grid spacing h. All results for this integral quantity converge to the exact solution with second-order behavior on the finest grid levels. Note that when using the compressible equations, it is necessary to remove the effect of variable density when post-processing drag to compare with the exact solution specified for incompressible flow.

It is important to note that although the absolute value of errors in drag coefficient are monotonically decreasing, the actual drag levels do not exhibit monotonic convergence until the finest three grid levels. This can be seen in Fig. 2. The c_d, GCI, and uncertainty on the finest grid level are listed in Table 1.

Table 1. The c_d and its uncertainty on the finest grid for MS1 on sg1

Code	Turbulence advection order	c_d	approx GCI, %	$U(c_d)$
CFL3D	2nd	0.644531×10^{-5}	3.05	0.196577×10^{-6}
CFL3D	1st	0.638512×10^{-5}	4.26	0.271690×10^{-6}
FUN3D	2nd	0.644844×10^{-5}	5.09	0.327975×10^{-6}
FUN3D	1st	0.637872×10^{-5}	7.67	0.489037×10^{-6}

Figs. 3 and 4 show L1-norm errors for various quantities, using second-order and first-order discretization for turbulence advection, respectively. In Fig. 3, convergence is second-order for all quantities, as expected. For Fig. 4, convergence degrades to first-order. Results on the sg2 grid (with finer normal spacing) are given in Fig. 5. Again, when the turbulence advection terms are discretized second-order, the global error norms for all quantities converge second-order. It should be noted in practice, however, that for most aerodynamic problems of interest, little practical influence of first-order treatment of the turbulence advection terms has been found using typical grids.

Fig. 6 shows the convergence of various flow field quantities at a specific location in the domain as a function of h both grid sets. Both codes are approaching the exact solution, with the sg2 series of grids generally converging in a "smoother" fashion than the sg1 series. Note that in some cases, the convergence is oscillatory (non-monotonic), even on the finest grid levels.

IV. Backward Facing Step Validation Case

The backward facing step case was run on the same series of hexahedral grids in both codes. Only the node-centered formulation of FUN3D was employed, and both codes were run using first-order discretization for turbulence advection. The finest grid consisted of $255,266$ grid points ($253,952$ cells), with minimum spacing at the bottom and top walls of 1.5×10^{-4}. This spacing yielded an approximate average y^+ at the first cell-center of about 0.25 on the finest grid. The grid was *not* clustered with viscous spacing along the back face of the step, however: minimum spacing there was 0.0208333. Successively coarser grids were constructed by removing every-other point in each coordinate direction. Fig. 7 shows the grid 3-levels-coarser than the finest grid (with only 3968 cells). The grid clustering from the upstream near-wall region continued into the shear layer, with some spreading.

All solid walls were solved as no-slip walls. In CFL3D these were treated as adiabatic, whereas in FUN3D they were given a constant temperature equal to the freestream adiabatic temperature. At the upstream boundary, the velocity and turbulence were specified according to the manufactured solution given by the workshop organizers. At the downstream boundary, pressure was specified ($p/p_{ref} = 1.00149$), and all other variables were extrapolated from the interior of the domain.

Convergence of various surface integral quantities with decreasing grid spacing h ($= \sqrt{1/N}$) is shown in Fig. 8. These drag coefficients are defined in the standard way, as a force divided by $q_\infty S_{ref}$, where $q_\infty = 1/2\rho_\infty u_\infty^2$. In previous uncertainty workshops, e.g., Eca et al.,[14] the drag forces were nondimensionalized without the $1/2$ factor in the denominator. As a result, the current drag results are a factor of 2 larger than earlier reported results. Both codes generally go to similar results as the grid is refined, although for $c_{d,v}$ on the bottom wall it is not clear whether the results will cross or stay together if the grid could be refined further.

Estimates of the uncertainty are also shown for the finest two grid levels. These estimates are computed using the methodology described earlier, using the grid level in question plus 2 coarser levels. For $c_{d,v}$ on the bottom wall, CFL3D is well-behaved with an apparent (approximately) second-order convergence, so its uncertainty levels are small; FUN3D on the other hand is converging at less than first-order according to the finest three grids, so its uncertainty for this quantity is higher. For $c_{d,v}$ on the top wall, CFL3D exhibits oscillatory convergence, whereas FUN3D is monotonically converging. Finally, both codes show well-behaved convergence and hence reasonable uncertainty levels for c_d, p. In this case, FUN3D appears closer to the grid-converged result on any given grid, so its uncertainty levels are smaller than those of CFL3D.

The reattachment location is shown in Fig. 9. It appears that both codes will yield a reattachment point on an infinitely-refined grid of approximately 6.02.

Table 2 gives values for the various integrated quantities as well as the reattachment point on the fine grid, along with the corresponding computed GCI and uncertainty.

Table 2. Various quantities and their uncertainty on the finest grid for backward facing step

Code	quantity	fine grid value	approx GCI, %	$U(c_d)$
CFL3D	$c_{d,v}$ bottom wall	0.0523858	0.07	0.342654×10^{-4}
	$c_{d,v}$ top wall	0.0944691	0.57	0.538355×10^{-3}
	c_p step	0.2010955	2.45	0.491621×10^{-2}
	reattachment	6.01137	0.26	0.0154735
FUN3D	$c_{d,v}$ bottom wall	0.0523199	2.69	0.140690×10^{-2}
	$c_{d,v}$ top wall	0.0940830	0.65	0.609768×10^{-3}
	c_p step	0.2061919	0.52	0.106451×10^{-2}
	reattachment	6.06012	0.70	0.0422834

Figs. 10, 11 and 12 show comparisons of wall pressure coefficient and skin friction coefficient with experiment. Fine grid results along with error bars for both CFD and experiment are shown. Results for the two codes are almost indistinguishable, but agreement with experiment is only marginal along the bottom wall. In particular, C_p is too low for CFD for $x < 3$, and C_f is too low for CFD both over the first half of the bubble as well as downstream of reattachment. Interestingly, the location for reattachment (where C_f passes through zero) appears to agree very well with the experimental location. Although not everywhere completely within the experimental error tolerance, the computed top wall pressure coefficients agree very well with experiment.

Finally, Figs. 13 - 21 show comparisons of profiles at 3 locations downstream of the step with experiment. Fine grid results along with error bars for both CFD and experiment are shown. Again, results for the two codes are almost identical. Generally speaking, computed results compare very well with experiment, with the notable exception of v-velocity at $x = 6H$, which is underpredicted significantly by the CFD.

V. Conclusions

Two RANS computer codes – FUN3D and CFL3D – have been analyzed using the manufactured solution MS1, then applied to a backward facing step computation and compared with experiment. For the manufactured solution on the finest grids, the expected asymptotic behavior was observed: discretization error was either first- or second-order

accurate, depending on the treatment of the turbulence advection term. Both codes converged appropriately to the exact solution, although sometimes with oscillatory-convergence behavior. For the backward facing step, both codes were again consistent with each other, in the sense that the solutions generally approached nearly identical results as the grid was refined. Comparisons with experiment included uncertainty estimates for both CFD and experiment.

References

[1]Anderson, W. K. and Bonhaus, D. L., "An Implicit Upwind Algorithm for Computing Turbulent Flows on Unstructured Grids," *Computers and Fluids*, Vol. 23, No. 1, 1994, pp. 1–22.

[2]Anderson, W. K. and Rausch, R. D. and Bonhaus, D. L., "Implicit/Multigrid Algorithms for Incompressible Turbulent Flows on Unstructured Grids," *Journal of Computational Physics*, Vol. 128, No. 2, 1996, pp. 391–408.

[3]Nielsen, E. J., "Aerodynamic Design Sensitivities on an Unstructured Mesh Using the Navier-Stokes Equations and a Discrete Adjoint Formulation," PhD Thesis, Virginia Polytechnic Institute and State University, Blacksburg, VA, 1998.

[4]Roe, P. L., "Approximate Riemann Solvers, Parameter Vectors, and Difference Schemes," *Journal of Computational Physics*, Vol. 43, 1981, pp. 357–372.

[5]Nielsen, E. J. and Lu, J. and Park, M. A. and Darmofal, D. L., "An Implicit, Exact Dual Adjoint Solution Method Implicit, Exact Dual Adjoint Solution Method for Turbulent Flows on Unstructured Grids," *Computers and Fluids*, Vol. 33, No. 9, 2004, pp. 1131–1155.

[6]Spalart, P. R., and Allmaras, S. R., "A One-Equation Turbulence Model for Aerodynamic Flows," *La Recherche Aerospatiale*, No. 1, 1994, pp. 5–21.

[7]Menter, F. R., "Two-Equation Eddy-Viscosity Turbulence Models for Engineering Applications," *AIAA Journal*, Vol. 32, No. 8, 1994, pp. 1598–1605.

[8]Krist, S. L. and Biedron, R. T. and Rumsey, C. L., "CFL3D User's Manual (Version 5.0)," NASA TM-1998-208444, June 1998.

[9]Celik, I. B., Ghia, U., Roache, P. J., Freitas, C. J., Coleman, H., and Raad, P. E., "Procedure for Estimation and Reporting of Uncertainty Due to Discretization in CFD Applications," *Journal of Fluids Engineering*, Vol. 130, July 2008, 078001.

[10]Eca, L. and Hoekstra, M., "Discretization Uncertainty Estimation Based on a Least Squares Version of the Grid Convergence Index," Proceedings of the 2nd Workshop on CFD Uncertainty Analysis, Instituto Superior Tecnico, Lisbon, October 2006.

[11]Eca, L., Hoekstra, M., Hay, A., and Pelletier, D., "On the Construction of Manufactured Solutions for One and Two-Equation Eddy-Viscosity Models," *Int. Journal for Numerical Methods in Fluids*, Vol. 54, 2007, pp. 119–154.

[12]White, F. M., *Viscous Fluid Flow*, McGraw-Hill, Inc., New York, 1974, p. 475.

[13]Speziale, C. G., Abid, R., and Anderson, E. C., "Critical Evaluation of Two-Equation Models for Near Wall Turbulence," *AIAA Journal*, Vol. 30, No. 2, 1992, pp. 324–331.

[14]Eca, L., Hoekstra, M., and Roache, P. J., "Verification of Calculations: an Overview of the 2nd Lisbon Workshop," AIAA Paper 2007-4089, June 2007.

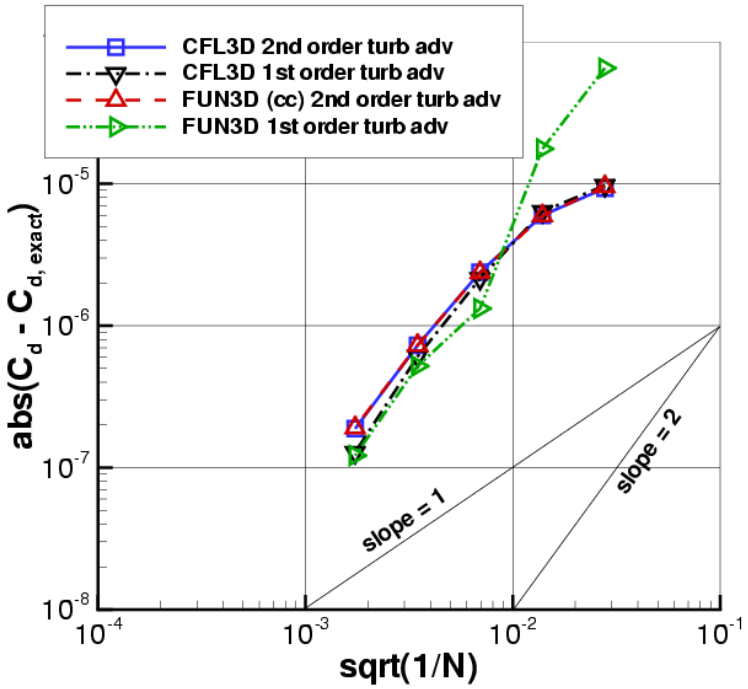

Figure 1. Error in drag coefficient for MS1 on sg1 as a function of h.

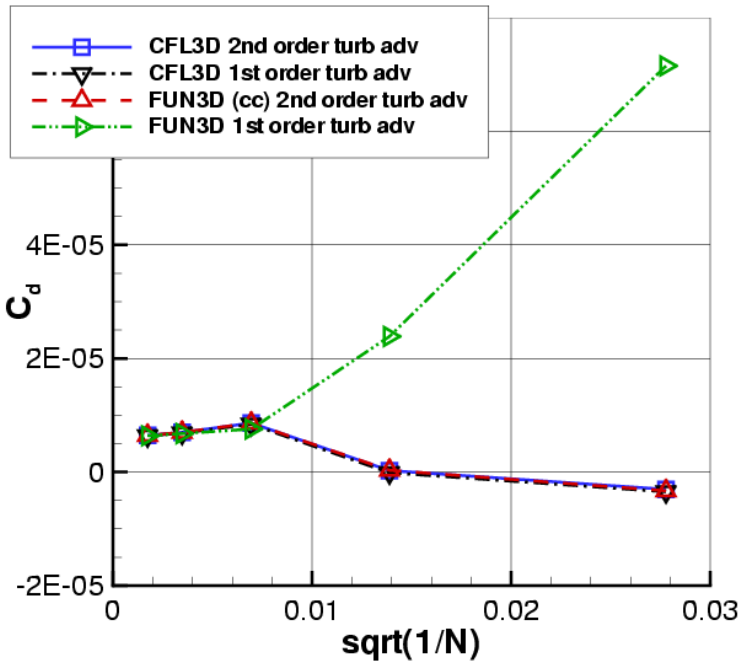

Figure 2. Drag coefficients for MS1 on sg1 as a function of h, showing oscillatory convergence on the coarsest two grid levels for three of the methods.

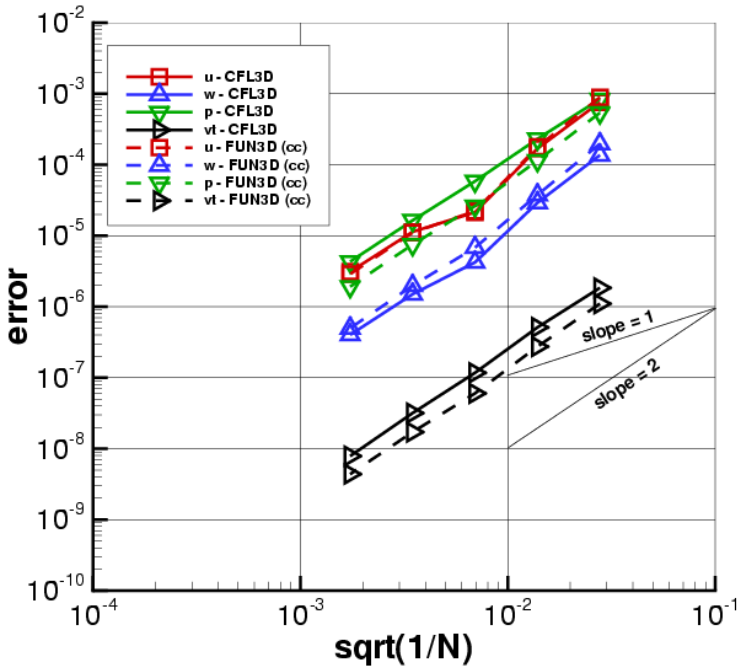

Figure 3. L1-norm of errors in u, v, p, and $\tilde{\nu}$ for MS1 on sg1 using FUN3D (cell-centered) and CFL3D, both with second-order discretization for turbulence advection.

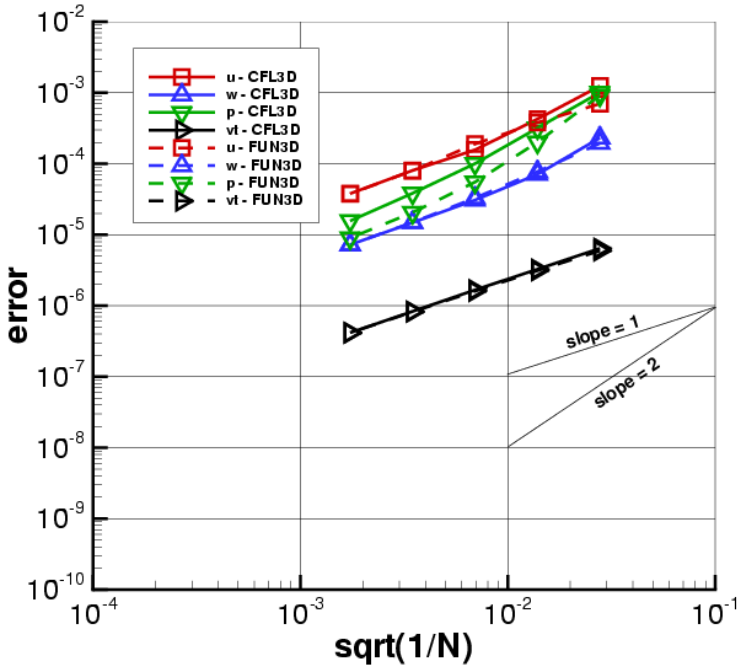

Figure 4. L1-norm of errors in u, v, p, and $\tilde{\nu}$ for MS1 on sg1 using FUN3D (node-centered) and CFL3D, both with first-order discretization for turbulence advection.

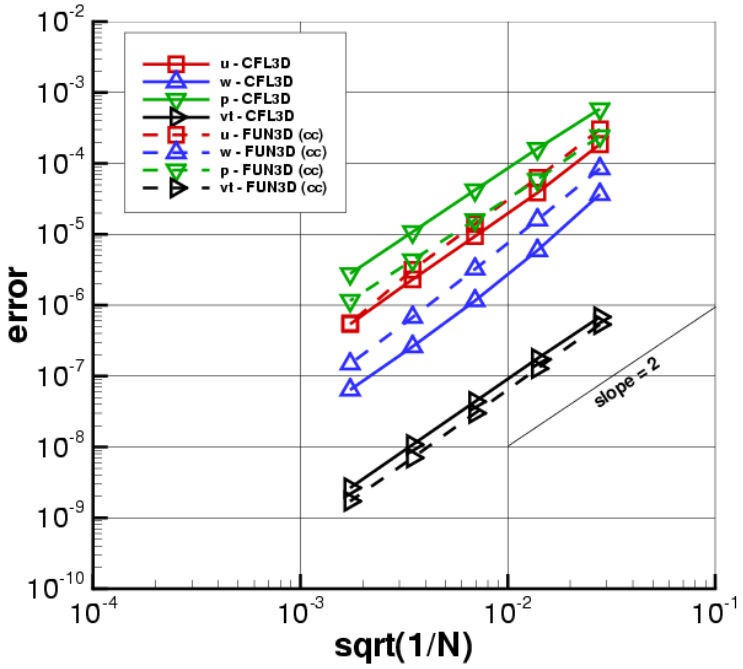

Figure 5. L1-norm of errors in u, v, p, and $\tilde{\nu}$ for MS1 on sg2 using FUN3D (cell-centered) and CFL3D, both with second-order discretization for turbulence advection.

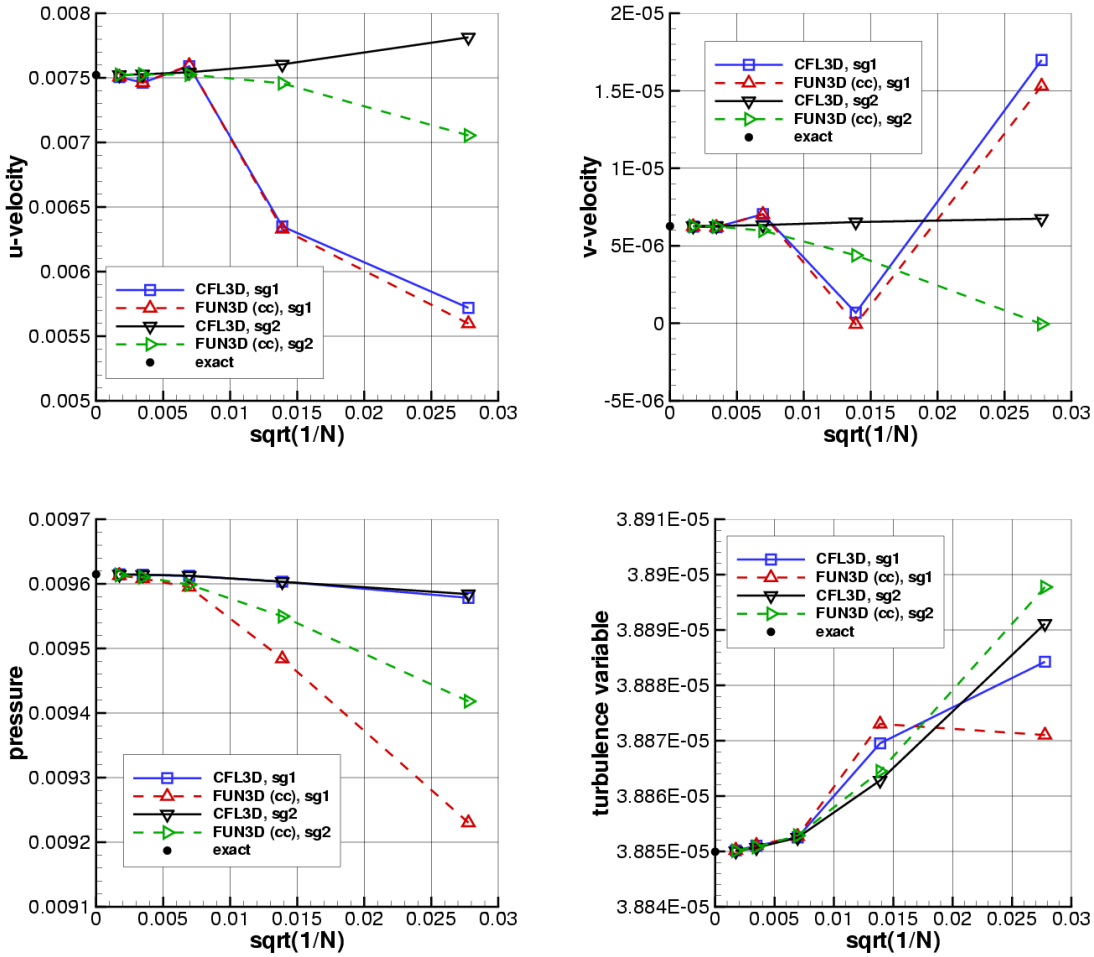

Figure 6. Convergence of various flow field quantities at $x = 0.6$, $y = 0.001$ for MS1 on sg1 and sg2 using FUN3D (cell-centered) and CFL3D, both with second-order discretization for turbulence advection.

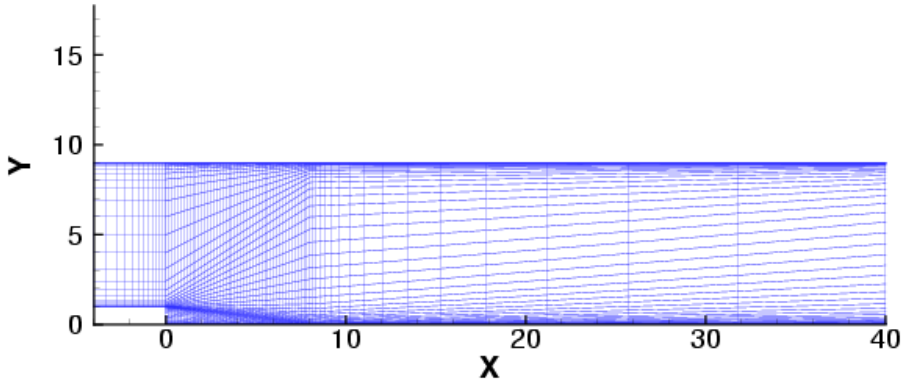

Figure 7. Hexahedral grid for the backward facing step case (showing only every 8th point in each coordinate direction for clarity).

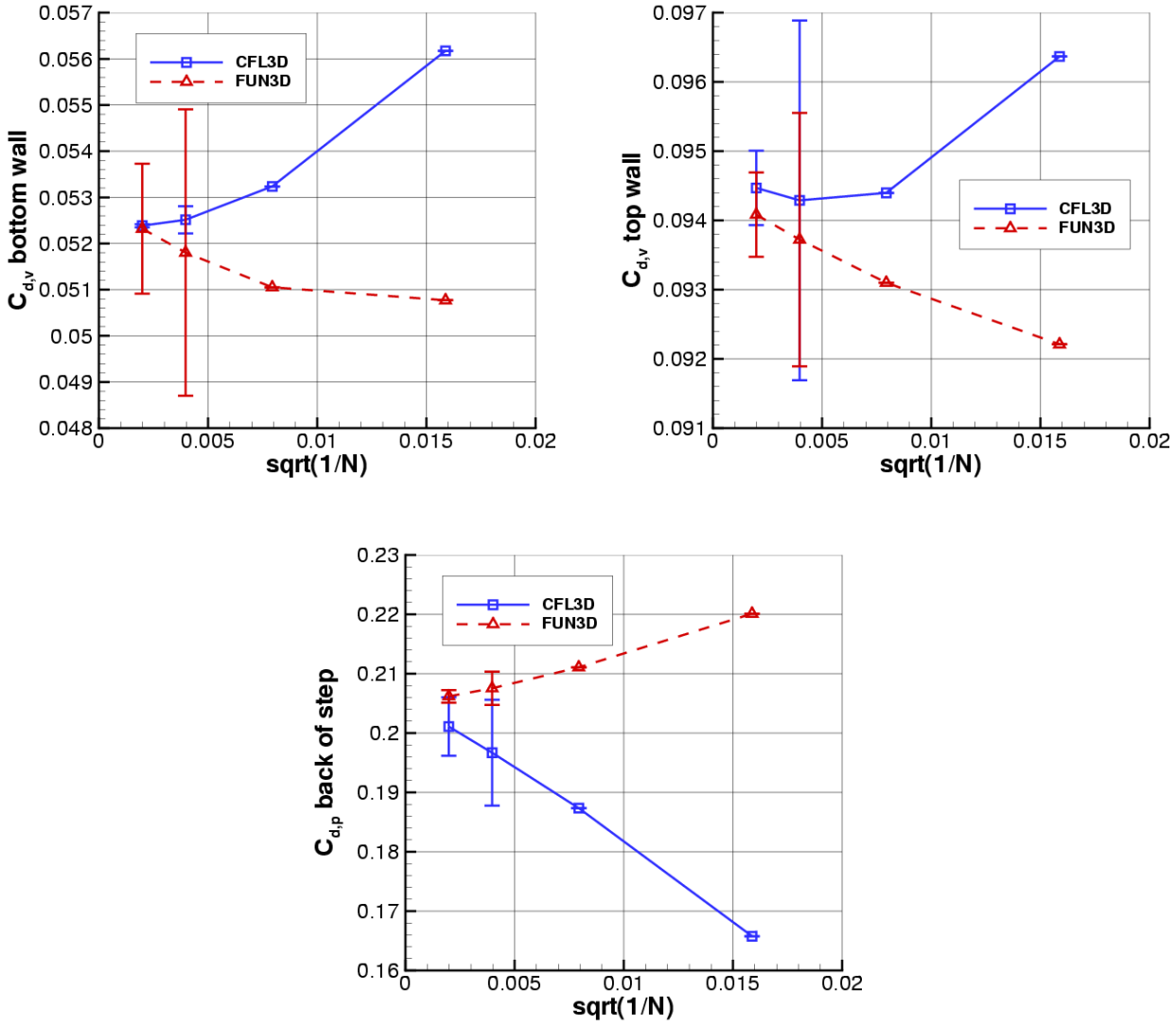

Figure 8. Convergence of various surface integral quantities, including uncertainty estimates on the finest 2 grid levels.

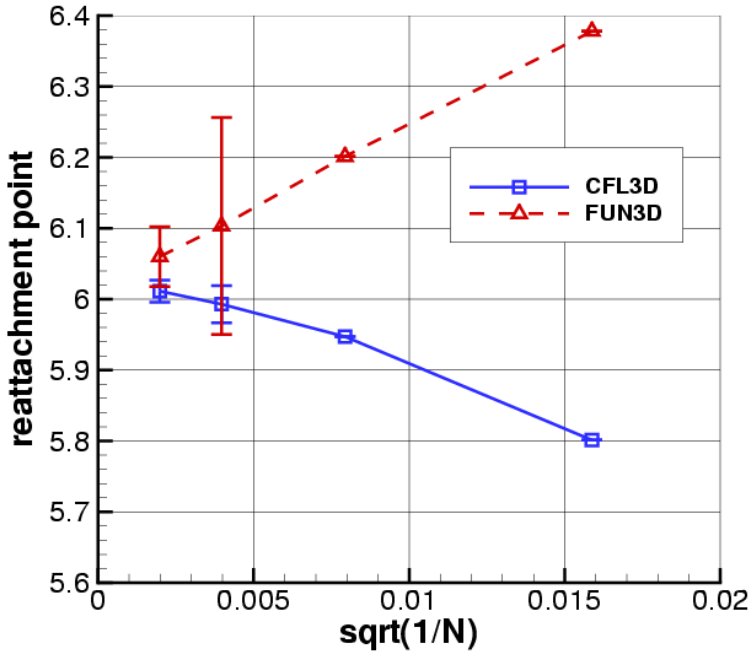

Figure 9. Convergence of reattachment location behind step, including uncertainty estimates on the finest 2 grid levels.

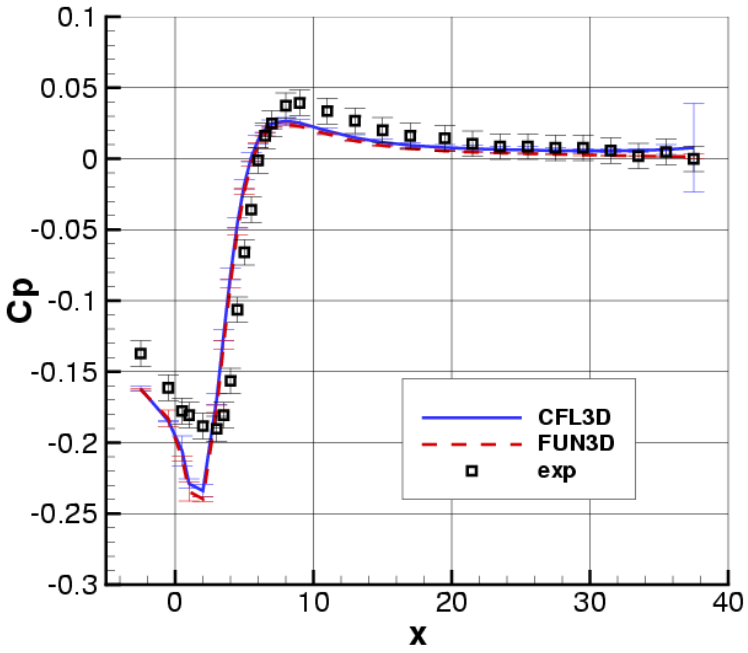

Figure 10. Surface pressure coefficient along the bottom wall, including uncertainty error bars for both CFD and experiment.

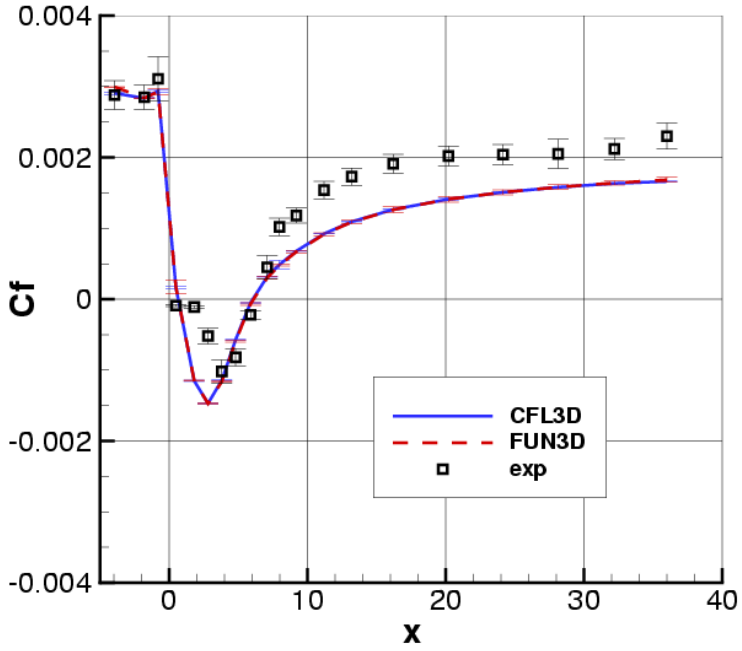

Figure 11. Surface skin friction coefficient along the bottom wall, including uncertainty error bars for both CFD and experiment.

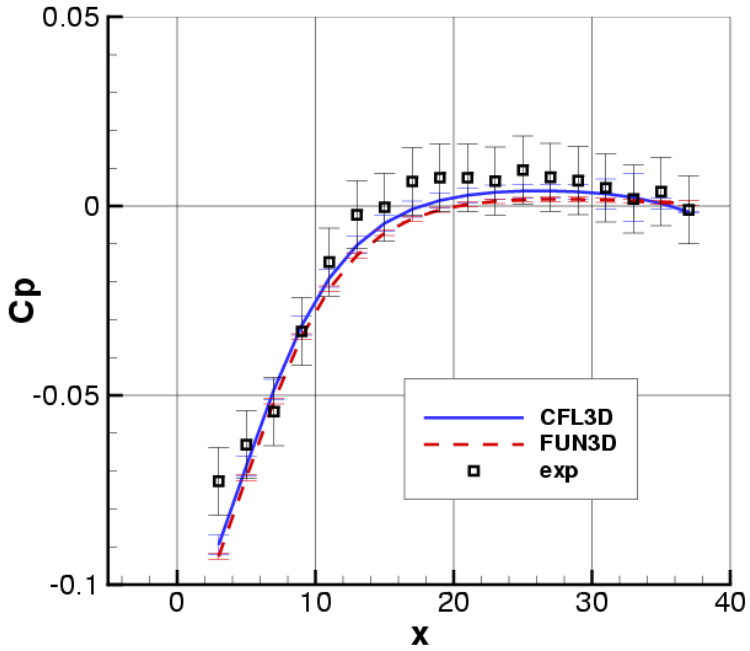

Figure 12. Surface pressure coefficient along the top wall, including uncertainty error bars for both CFD and experiment.

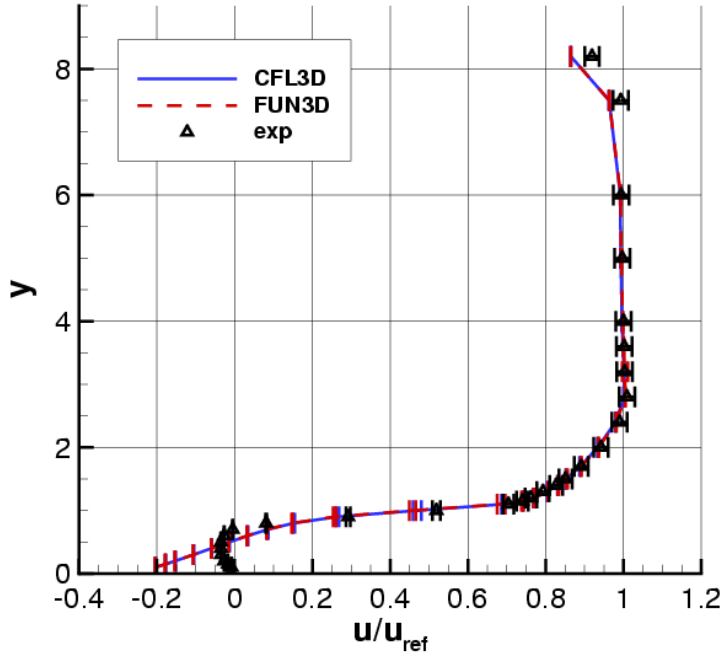

Figure 13. Profiles of u/u_{ref} at $x = 1H$, including uncertainty error bars for both CFD and experiment.

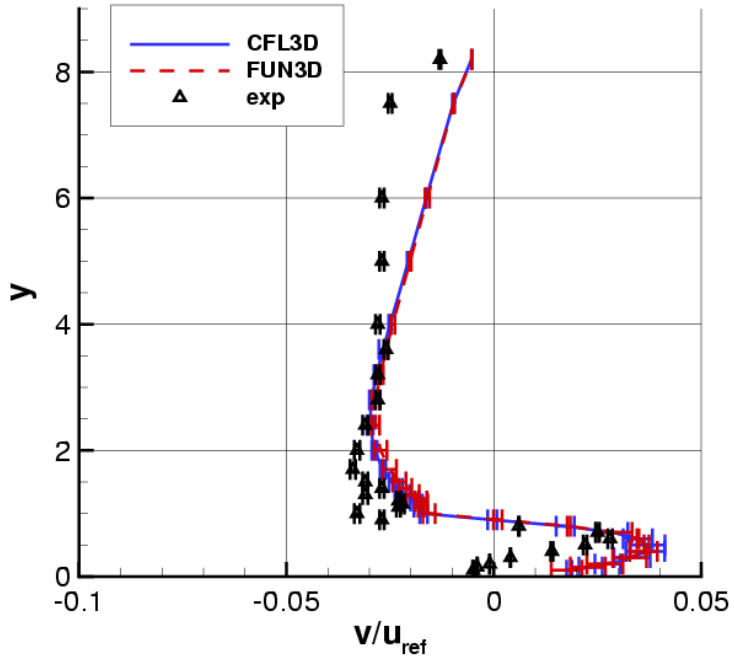

Figure 14. Profiles of v/u_{ref} at $x = 1H$, including uncertainty error bars for both CFD and experiment.

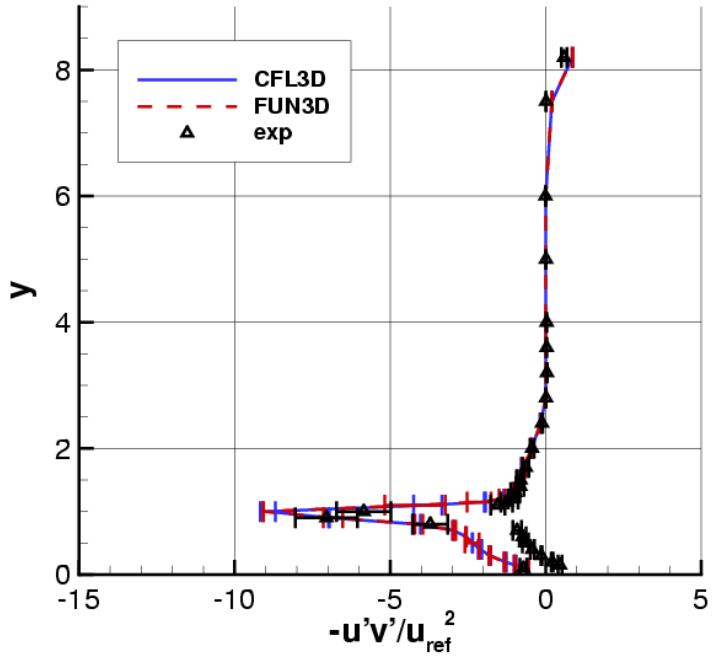

Figure 15. Profiles of $u'v'/u_{ref}^2$ at $x = 1H$, including uncertainty error bars for both CFD and experiment.

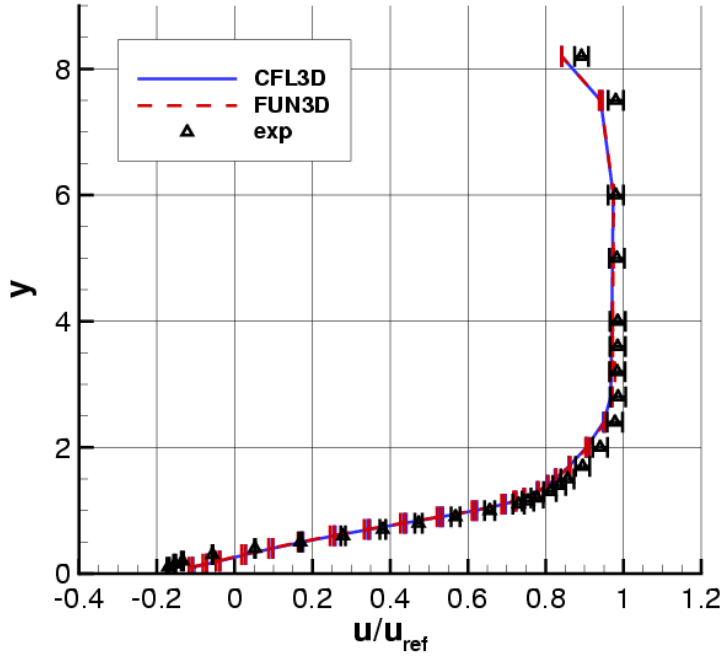

Figure 16. Profiles of u/u_{ref} at $x = 4H$, including uncertainty error bars for both CFD and experiment.

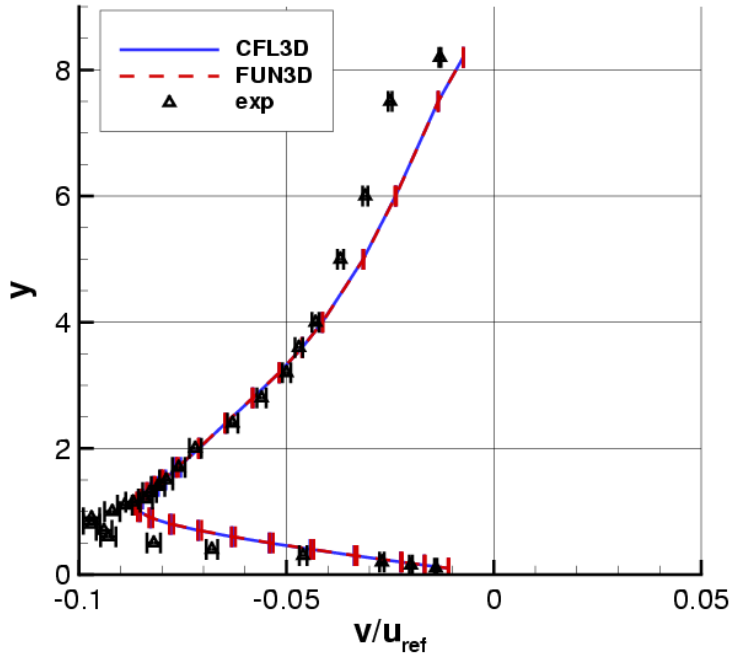

Figure 17. Profiles of v/u_{ref} at $x = 4H$, including uncertainty error bars for both CFD and experiment.

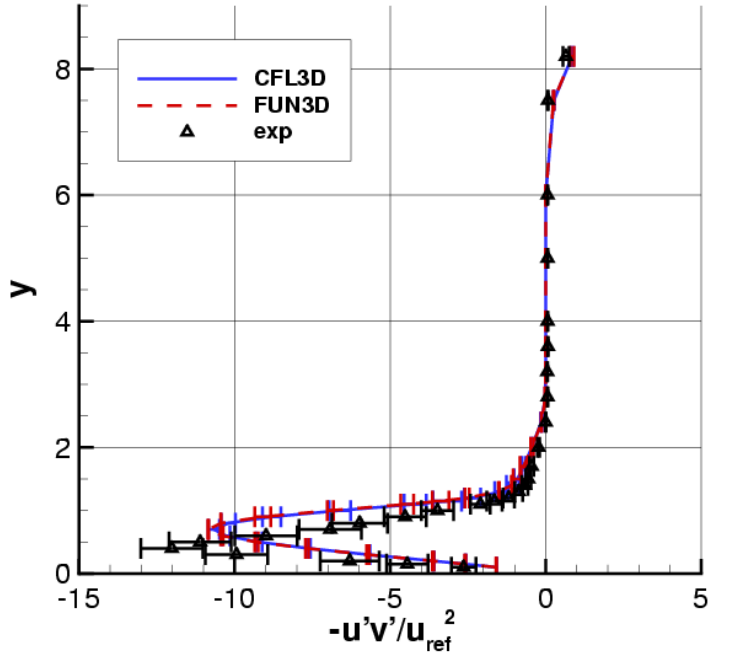

Figure 18. Profiles of $u'v'/u_{ref}^2$ at $x = 4H$, including uncertainty error bars for both CFD and experiment.

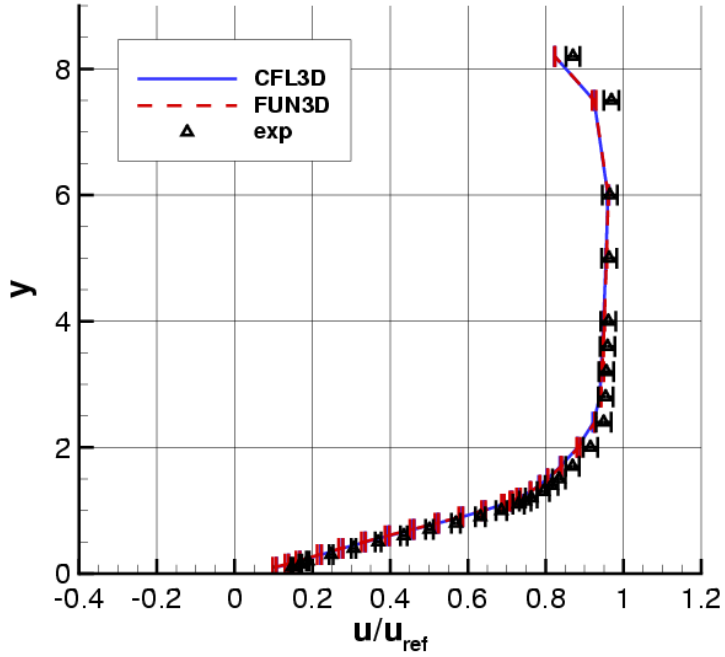

Figure 19. Profiles of u/u_{ref} at $x = 6H$, including uncertainty error bars for both CFD and experiment.

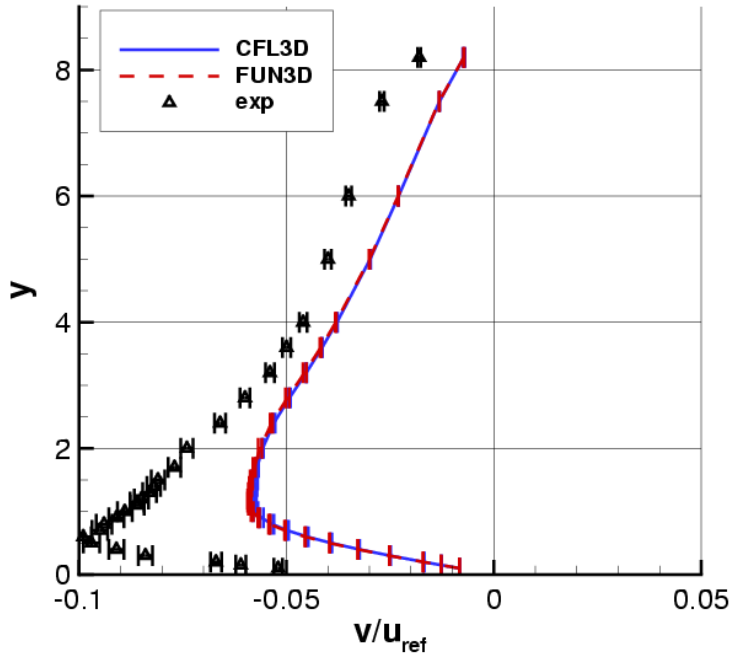

Figure 20. Profiles of v/u_{ref} at $x = 6H$, including uncertainty error bars for both CFD and experiment.

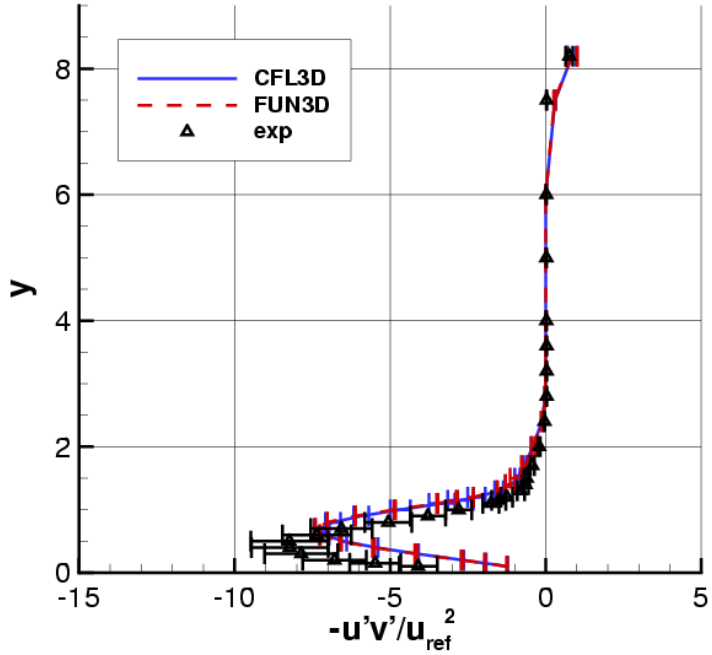

Figure 21. Profiles of $u'v'/u^2_{ref}$ at $x = 6H$, including uncertainty error bars for both CFD and experiment.